ACS APPLIED BIO MATERIALS

www.acsabm.org Article

Eyeball-Like Yolk–Shell Bimetallic Nanoparticles for Synergistic Photodynamic–Photothermal Therapy

Xiaoli Cai,[‖] Shichao Ding,[‖] Qiurong Shi, Zhaoyuan Lyu, Dong Liu, Wen-ji Dong, Min Du, Prashanta Dutta, Yang Song,* Dan Du,* and Yuehe Lin*

Cite This: *ACS Appl. Bio Mater.* 2020, 3, 5922–5929 Read Online

ACCESS | Metrics & More | Article Recommendations | Supporting Information

ABSTRACT: Noble metal-based nanomaterials offer great potential as cargoes for multifunctional cancer treatment. In this research, Au eyeball-like nanoparticles (NPs) with open-mouthed Pd shells were synthesized and their surface was functionalized with cell-targeting ligand folic acid (FA) and photodynamic agent Chlorin e6 (Ce6). Due to the broad near-infrared (NIR) absorption band of eyeball-like bimetallic Au and Pd, the photothermal therapy effects of this nanomaterial were studied in MCF-7 cancer cells. The anchored Ce6 not only addressed the hypoxia issue of tumor cells but also exhibited remarkable photodynamic efficacy upon irradiation. Results showed that the obtained Au@Pd-PEG-FA-Ce6 (APPFC) NPs were selectively accumulated at the tumor site and induced cell apoptosis effectively due to the target specificity and synergistic phototherapy effect. The high specificity, desirable biosafety, fast delivery, and drug functionalization demonstrated eyeball-like Au@Pd NPs are promising candidate for multifunctional therapy of breast cancer.

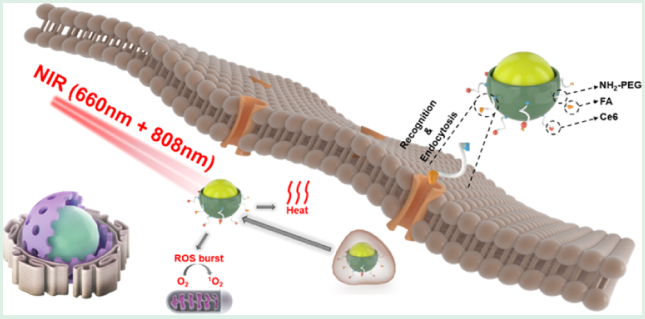

KEYWORDS: *Au@Pd nanoparticles, folic acid, Chlorin e6, multifunctional therapy, breast cancer*

INTRODUCTION

Breast cancer, a devastating tumor disease, not only has the highest incidence rate but also is the reason for the second-highest death rates in females.[1] To break this hard nut, phototherapy has been regarded as a promising cancer therapeutic modality and inevitably attracted huge attention by numerous scholars in the past few decades.[2−6] There are primarily two types of phototherapy approaches for cancer treatments: photodynamic therapy (PDT) and photothermal therapy (PTT).[7−10] PDT uses photosensitizers (PSs) to produce reactive oxygen species (ROS) with a specific wavelength of light, and the generated ROS can destroy nearby cancer cells.[11] PTT, on the other hand, uses photoabsorbing agents to destroy tumors with hyperthermia produced by near-infrared (NIR) laser irradiation.[12] Nevertheless, highly efficient phototherapy remains limited due to various drawbacks associated with current techniques. For example, it is difficult to eradicate tumors by single PTT effect completely, especially for tumors located deep into the tissues due to a significant depth-dependent decrease of the NIR laser intensity.[13] Moreover, related nanotherapeutics are hampered by the insufficient loading of PSs, nonspecificity, and low biosafety.[14,15]

Most recently, multifunctional noble metal-based nanomaterials have provided opportunities to improve therapeutic efficacy by overcoming the disadvantages of PDT and PTT.[16,17] Among them, gold (Au) nanomaterials with diversified morphologies are usually selected as ideal PTT candidates due to their localized surface plasmon resonance absorption (SPR) band in the NIR region.[18−20] For example, Qi and co-workers presented Au nanoparticle-based nanotheranostic probe and investigated its SPR effect for PTT of cancer.[21] In the latest achievements by Shieh's group,[22] Au nanoparticles were also used as nanoplatforms to deliver dichloro(1,2-diaminocyclohexane)platinum(II) (DACHPt) for combined chemo-photothermal therapy in colorectal cancer. Au nanomaterials not only can transfer photo energy into thermal energy for photothermal therapy but also can utilize tunable SPR under NIR laser irradiation condition that further enhances their potential in biomedical applications.[23,24] An effective strategy for red-shifting the absorption band to the NIR region is by incorporating other metals to exploit the synergistic effects between compounds strategically. Palladium (Pd), another common noble metal, has already been employed as an active potential material for cancer treatment

Received: May 25, 2020
Accepted: July 7, 2020
Published: July 7, 2020

https://dx.doi.org/10.1021/acsabm.0c00624
ACS Appl. Bio Mater. 2020, 3, 5922–5929

due to its unique features and remarkable properties.[25] For example, Pd could supply a wider bio window in the NIR region as well as enhance the PTT effect.[26] It is expected that if the Pd element can be hybridized with other metals, one can overcome the weaknesses of single counterparts leading to an optimized performance in cancer treatment. In this work, we designed eyeball-like Au@Pd nanoparticles (NPs): a Au sphere core surrounded by a bowl-like thin Pd nanolayer (Scheme 1).

Scheme 1. Schematic View of the Synthesis Process for the APPFC Drug Delivery System and Subsequent Cellular Uptake for the Effective Cancer Cell Treatment

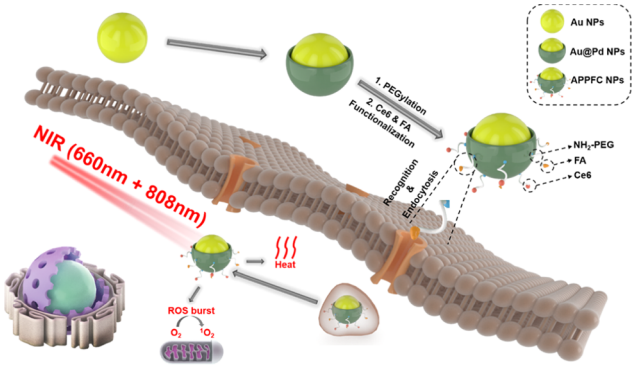

Compared to a closed yolk−shell structure,[27] these eyeball-like yolk−shell Au@Pd NPs could exhibit favorable properties of both Au and Pd by providing high SPR-enhanced properties in the NIR region.

Apart from enhancing the therapeutic effect, it is also essential to enhance the specificity and desirable biocompatibility of the eyeball-like yolk−shell Au@Pd drug delivery system.[28−32] Several biomimicry strategies are generally used to ensure their proper biosafety both *in vivo* and *in vitro*, such as "Self" peptides, cell membrane coating, "Leukolike" coating, and PEGylation.[33−35] Among them, PEGylation is more straightforward and efficient as biomimicry strategy. In light of this, we functionalized the designed eyeball-like Au@Pd NPs by PEGylation processing. In addition, we anchored photodynamic agent Chlorine e6 (Ce6) as well as targeting ligand folic acid (FA) for treating breast cancer MCF-7 cells (Scheme 1). The high surface area-to-mass ratio of Au@Pd NPs has resulted in loading of high therapeutic photodynamic agents and targeted ligand molecules on the shell. The treatment effects of PTT and PDT were thoroughly evaluated *in vitro* microenvironments. This eyeball-like yolk−shell Au@Pd system exhibits excellent solubility, higher drug loading capacity, better photothermal efficacy, and higher specificity, which was employed for synergistic targeted and dual photodynamic−photothermal breast cancer therapy.

RESULTS AND DISCUSSION

All types of NPs were successfully prepared and well characterized. The designed route for preparing Au@Pd NPs is illustrated in Scheme 1. The structures and morphologies at each step were performed using transmission electron microscopy (TEM). As shown in Figure 1a,b, the 12 nm sized Au nanoparticles have ∼4 nm thick Ag. Further morphological characterization demonstrated that the yielded Au@Pd NPs exhibited an eyeball-like yolk−shell structure (Figure 1c,d).[36,37] Although the yielded Au@Pd NPs were initially water-soluble, they quickly aggregated in the phosphate-buffered saline (PBS) solution due to the electron screening effect, indicating their instability in human physiological conditions (Figure S1). Therefore, the surface modification of eyeball-like Au@Pd NPs is needed before introducing them in cancer therapy. Poly(ethylene glycol) (PEG) grafting is one of the most common strategies for surface passivation to enhance stability and reduce the electron screening effect.[38] In our system, we used diamino-terminated PEG to functionalize these eyeball-like Au@Pd NPs owing to the amino group that could effectively bind to Au@Pd NPs to obtain Au@Pd-PEG NPs.[39] The PEG grafting improved the physiological stability of Au@Pd NPs in PBS, even after keeping them at room temperature for 3 days (Figure S2). Dynamic light scattering measurements also verified the size distribution of Au@Pd NPs (Figure 1e) and Au@Pd-PEG NPs (Figure S3). Although the original Au@Pd NPs and the ones after PEGylation showed ∼40 nm difference in average

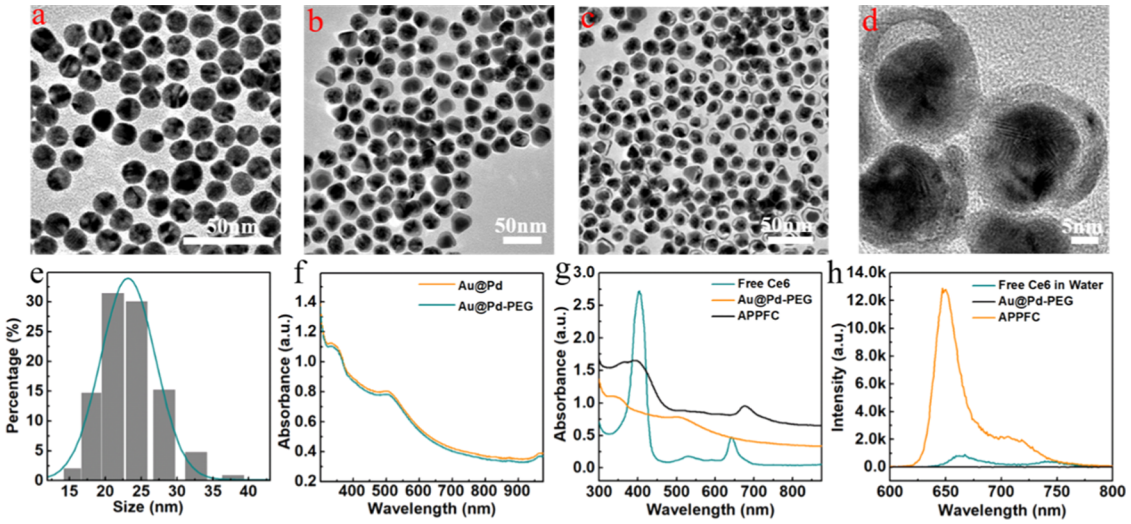

Figure 1. TEM of as-prepared Au NPs (a) and Au@Ag NPs (b); TEM of eyeball-like Au@Pd NPs (c, d); size distribution of Au@Pd NPs as measured by dynamic light scattering (e); UV−vis absorbance spectra of Au@Pd NPs and Au@Pd-PEG NPs (f); UV−vis absorbance spectra (g) and fluorescence spectra (h) of Ce6, Au@Pd-PEG, and Au@Pd-PEG-FA-Ce6 (APPFC) in water.

https://dx.doi.org/10.1021/acsabm.0c00624
ACS Appl. Bio Mater. 2020, 3, 5922−5929

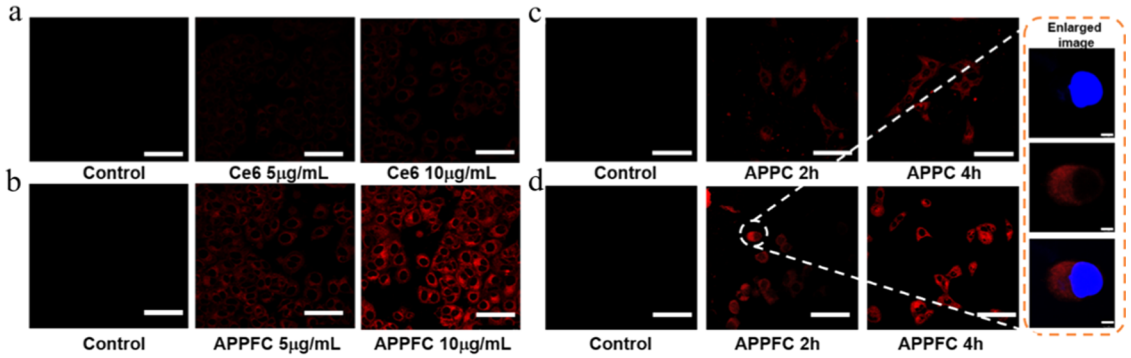

Figure 2. CLSM images of MCF-7 cells incubated with different concentrations of Ce6 (a) and Au@Pd-PEG-FA-Ce6 (APPFC) (Ce6 amount: 5 or 10 μg mL^{-1}) (b); CLSM images of MCF-7 cells incubated with APPC (c) and APPFC (d) under different times. Scale bars of the CLSM image and enlarged image are 75 and 5 μm, respectively.

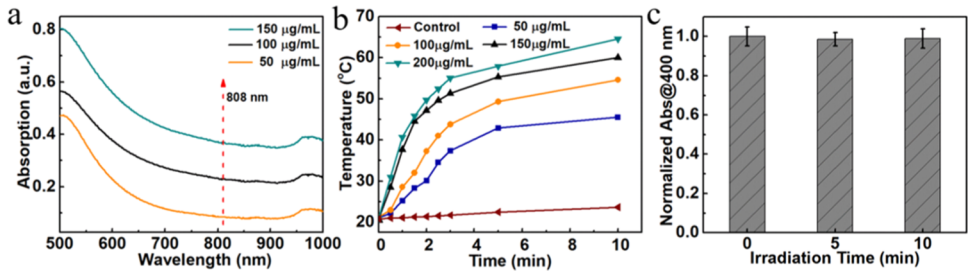

Figure 3. UV−vis adsorption intensity of APPFC for different concentrations (a); transient temperature profile for different concentration (1.5 W cm^{-2} NIR at 808 nm) (b); and photothermal stability of APPFC (c).

diameter, the exhibited durable UV to NIR absorbance spectra were not affected by the PEG surface modification (Figure 1f).

The UV−vis and fluorescence characterization of Au@Pd-PEG and Au@Pd-PEG-FA-Ce6 (APPFC) further demonstrated that Au@Pd NPs have been successfully functionalized with photodynamic agents (Figure 1g). Compared with the absorbance of Au@Pd-PEG NPs, the UV−vis spectra of APPFC NPs showed the characteristic absorption peaks of Ce6 (a Soret peak in 405 nm and a *Q* band in 675 nm). The successful loading of Ce6 into Au@Pd NPs also provided a visible color change from wine-red to dark yellow (Figure S2c,d). Herein, the loading capacity of Ce6 on Au@Pd-PEG was also determined and found to be 36% (testing process and calculation method are illustrated in the Supporting Information). Besides, FA peaks were observed from the UV−vis absorbance spectra of APPFC (Figure S4), which confirmed the conjugation of FA. Furthermore, the fluorescence intensity from Ce6 on APPFC NPs was found to be higher than that of free Ce6 in water (Figure 1h). This higher fluorescence intensity can be attributed to the increased dispersibility owing to the prevention of usual $\pi-\pi$ stacking of Ce6 in aqueous solution after conjugation on the surface of Au@Pd NPs, which is very desirable for further testing in cell physiological condition.[40]

To test whether Au@Pd-PEG NPs facilitated PSs to enter cancer cells, confocal laser scanning microscopy (CLSM) experiments were performed on breast cancer cells to determine the cellular internalization of Ce6 (Figure 2). Figure 2b showed the red fluorescence of Ce6 when MCF-7 cells were incubated with APPFC NPs (5 μg mL^{-1} of Ce6) for 4 h, while other cells, including those incubated with Ce6 alone (Figure 2a), did not show any signal. This could be attributed to the hydrophobic property of Ce6, which lowered the transport and usage efficiency of free Ce6 in the water-based cellular media.[40] These experimental data confirm that our functionalized APPFC NPs facilitate transportation of Ce6 in cancer cells. Moreover, the intensity of the red fluorescence signal also enhanced along with the increasing concentration of Ce6 (Ce6, 10 μg mL^{-1}) in APPFC (Figure 2b), suggesting that the APPFC system exhibited a concentration-dependent internalization in MCF-7 cells. In contrast, the fluorescence intensity of MCF-7 cells incubated with free Ce6 was weaker than that incubated with APPFC under the same Ce6 concentration (Figure 2a), which could be due to the target delivery of Ce6 in APPFC systems via receptor-mediated endocytosis.

As a useful targeting ligand, FA can recognize their receptors-overexpressed cells, specifically targeting MCF-7 cells in this work.[41,42] To assess the specific binding properties of FA modified eyeball-like Au@Pd NPs, MCF-7 cells were incubated with APPFC and APPC for different times, respectively. Here, MCF-7 cells exhibited an obvious red fluorescence signal of Ce6 in the cytoplasm after 2 h of incubation under the presence of APPFC (Figure 2d), which was clearly visible in zoom-in and merged images. Furthermore, the red fluorescence became brighter when treatment duration prolonged to 4 h, which demonstrated a time-dependent cellular internalization of APPFC NPs toward MCF-7 cells. Compared with the APPFC system (Figure 2d), the cells incubated with APPC NPs showed weaker red signals for both 2 and 4 h of incubation (Figure 2c), likely due to the absence of FA. Therefore, boosted by the inclusion of the targeting ligand, the eyeball-like bimetallic NPs exhibited a highly selective specificity toward MCF-7 cells.

UV−vis spectra were used to assess the photothermal effect of eyeball-like APPFC NPs. As shown in Figure 3a, they

https://dx.doi.org/10.1021/acsabm.0c00624
ACS Appl. Bio Mater. 2020, 3, 5922−5929

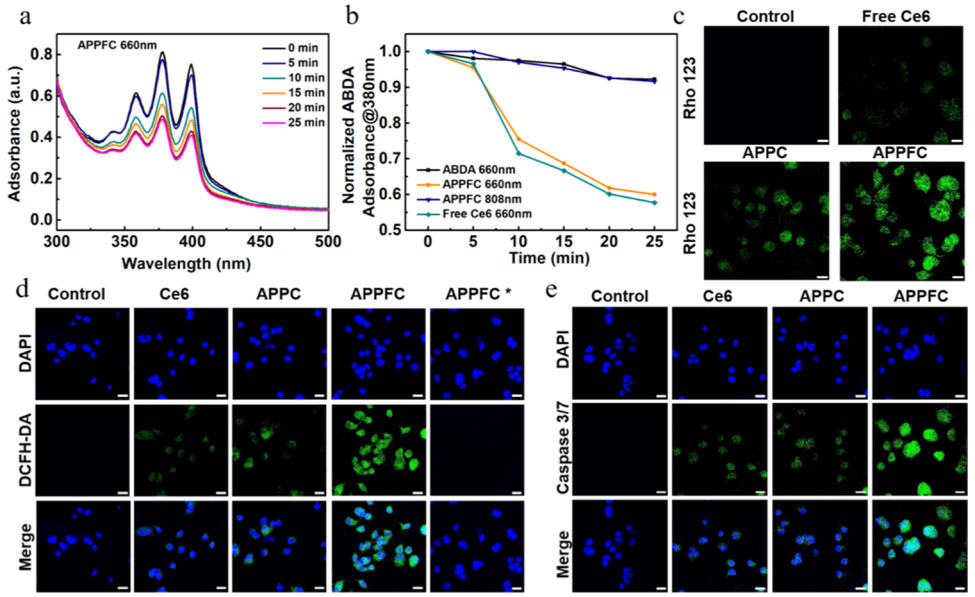

Figure 4. UV−vis absorption spectra of ABDA under 660 nm laser irradiation for different times in the presence of APPFC NPs (a); photodegradation rates of ABDA with a laser in the presence of free Ce6 and APPFC under 660 or 808 nm (b); CLSM images of ROS generation in MCF-7 cells treated with different agents with the laser. The intracellular ROS generation detected by the Rho 123 (c), DCFH-DA (d), and caspase 3/7 kit (e) after incubation with free Ce6, APPC NPs, or APPFC NPs. All laser irradiation was performed for 5 min at 660 nm with 50 mW cm^{-2} power except the APPFC* at 808 nm with 1.5 W cm^{-2}. (All scale bars of CLSM image are 25 μm.)

exhibited remarkably well NIR absorbance (808 nm) and the absorption intensity increased with changes in their concentrations. Figure 3b investigated the photothermal performance of APPFC for different concentrations. After laser irradiation with 808 nm, the temperatures of solutions containing APPFC were measured. As shown in Figure 3b, the temperature of APPFC increased when the concentration of APPFC or irradiation time increased. Moreover, these time-dependent photothermal heating effects of APPFC indicated that the photothermal temperature could exceed 50 °C in NIR laser heating (808 nm, 1.5 W cm^{-2}) for concentration above 100 μg mL^{-1}. Such high temperature may lead to sufficient cell damage.[9] To evaluate the photothermal stability of APPFC, we tested the UV−vis spectra of APPFC at 808 nm after different laser irradiation time (Figure 3c). Experimental results showed slight variations with irradiation time, indicating excellent photothermal stability of the APPFC system, which made them good candidates for further development in phototherapy applications *in vitro* and *in vivo*. Next, we used the Live−Dead Kit to investigate the photothermal effect of APPFC by evaluating the cell viability of MCF-7 cells under different treatments. As shown in Figure S5, the cell line was barely influenced in the area without exposure to the laser (the bottom area). However, significant cell death was observed when cells were treated with 808 nm laser irradiation, indicating the killing of cancer cells during photothermal therapy.

To study the ROS generation in this system, free Ce6 and APPFC were treated with laser irradiation for a different time and 9,10-anthracenediyl-bis-(methylene) dimalonic acid (ABDA) was used as an indicator (Figures 4a and S6). As shown in Figure S6, for 660 nm laser irradiation, there is a negligible change in ABDA absorbance (Figure S6a) when there was no ROS agent. A similar phenomenon was also observed for APPFC with an 808 nm laser (Figure S6c), suggesting that the introduction of 808 nm laser irradiation had a negligible effect on the ROS generation in APPFC. In contrast, when ABDA solutions containing free Ce6 (Figure S6b) or APPFC (Figure 4a) were exposed to 660 nm laser irradiation, the absorbance of ABDA decreased obviously, indicating only 660 nm laser irradiation could trigger the ROS generation by free Ce6 or APPFC NPs. Figure 4b presents the results of ABDA absorbance decrease at different wavelengths. Here, only a negligible difference was observed between free Ce6 and APPFC under 660 nm laser irradiation, suggesting that the APPFC NPs could effectively maintain the photodynamic activity of Ce6 in their structure.

Intracellular ROS generation was evaluated by a ROS fluorescence probe 2′,7′-dichlorofluorescein diacetate (DCFH-DA). As shown in Figure 4d, MCF-7 cells exhibited negligible green fluorescence when incubated with high free Ce6. However, obvious green fluorescence could be observed in MCF-7 cells after incubation with APPC, implying the massive intracellular ROS production by Ce6 in APPC. Furthermore, the green fluorescence signal inside the cells became much stronger than other groups when MCF-7 cells incubated with APPFC. This is due to the rapid transitivity, specific targeting of FA, and high stability of the APPFC nanomedicine system. Besides, to verify the laser trigger specificity, MCF-7 cells were incubated with APPFC NPs and treated with 808 nm laser irradiation (denoted as APPFC*). As expected, there was no fluorescence signal observed, suggesting that 808 nm laser irradiation was less efficient. This systematic experimental study shows that the APPFC nanosystem has the ability to generate ROS in *in vitro* system while heated with 660 nm laser irradiation and the targeted heating can improve the therapeutic efficacy of photodynamic therapy.

The ROS burst could break up the normal physiological redox state and further result in the destruction of mitochondrial membrane potential (MMP) and cell apoptosis. Hence, the MMP indicator rhodamine 123 (Rho 123) was utilized to assess the MMP condition in MCF-7 cells (Figure

https://dx.doi.org/10.1021/acsabm.0c00624
ACS Appl. Bio Mater. 2020, 3, 5922−5929

4c).[43] As shown in Figure 4c, MCF-7 cells emitted more robust green fluorescence when they were incubated with APPFC NPs than others (free Ce6 or APPC). The intensity of the green fluorescence is a direct measure of mitochondria destruction, suggesting the superior role of APPFC NPs in cancer treatment. In addition, we further evaluated the apoptosis of cells using the caspase 3/7 kit (Figure 4e) since the activation of caspase 3/7 is another crucial signal for cell apoptosis.[40] The intensity of caspase fluorescent signal was much stronger when the MCF-7 cells were incubated with APPFC NPs. This further demonstrates the excellent therapy effect of functionalized eyeball-like Au@Pd nanomaterials.

To demonstrate the superior treatment behavior of eyeball-like Au@Pd NPs by combing photothermal therapy and photodynamic therapy, we investigated the cell viability based on live/dead cell staining shown in Figure 5. When the cells

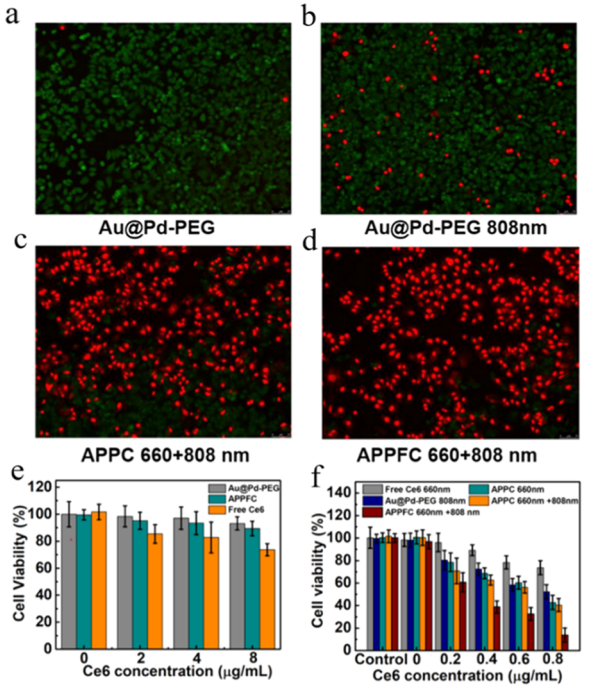

Figure 5. CLSM images of cell viability treated with Au@Pd-PEG (a), Au@Pd-PEG with 808 nm irradiation (b), APPC (c), and APPFC (d) under combined laser conditions (660 nm + 808 nm). The cells were stained with the live/dead viability kit. Green: live cells, red: dead cells. All laser irradiation was performed for 5 min. MTT assay of MCF-7 cells incubated with Au@Pd-PEG, free Ce6, and APPFC (various concentrations of Ce6) without irradiation (e) and under different irradiation (f).

were incubated with Au@Pd-PEG and treated with 808 nm laser irradiation, the red fluorescence of dead cells increased slightly (Figure 5b), indicating moderate PTT efficacy of Au@Pd-PEG. On the other hand, almost all cells showed red fluorescence when incubated with APPC NPs and treated with both 660 and 808 nm laser irradiations (Figure 5c), demonstrating synergistic effects of PTT and PDT in killing cancer cells. Furthermore, our experimental results suggest that the APPFC system has the higher lethality toward MCF-7 cells than that of APPC under identical irradiation conditions owing to the target specificity of FA (Figure 5d).

To further demonstrate the effects of PTT and PDT of this system against MCF-7 cancer cells, 3-(4,5-dimethylthiazo-2-yl)-2,5-di-phenyltetrazoliumromide (MTT) assay was conducted. First, the cytotoxicity of Au@Pd NPs before and after PEGylation was investigated. As shown in Figure S7, Au@Pd NPs exhibited cytotoxicity toward MCF-7 cells in high concentration but Au@Pd-PEG NPs showed negligible cytotoxicity toward MCF-7 cells even at high concentration of 100 μg mL^{-1}, revealing that Au@Pd-PEG NPs had good biocompatibility. After Ce6 loading and FA conjugation, APPFC also showed a low cytotoxic effect on MCF-7 cells without laser irradiation even at high Ce6 concentration (Figure 5e).

Figure 5f demonstrates the viability of cells treated with free Ce6, Au@Pd-PEG, APPC, and APPFC after different irradiation processes. As we can see, Au@Pd-PEG was able to induce partial cell death under 808 nm laser irradiation due to the PTT effect. Besides, free Ce6 and APPC exhibited concentration-dependent PDT effect under 660 nm laser irradiation, and the cell viability decreased to 68.3 and 46.2% at the concentration of 0.8 μg mL^{-1} Ce6, respectively (Figure 5f). Here, the viability of APPC-treated cells was significantly lower than that of free Ce6-treated cells because of the higher ROS generation in APPC NP incubated cells. The viability of APPC-treated cells was dramatically decreased under the combined laser irradiation (660 nm, 50 mW cm^{-2} and 808 nm, 1.5 W cm^{-2}), which demonstrated the successful combination of photothermal/dynamic therapy. Moreover, FA targeting further enhanced the treatment efficiency, which was illustrated by the lower cell viability (~13.7%) of APPFC treated cells than that of APPC-treated cells under the combined laser irradiation. These results confirmed that the designed APPFC system could kill MCF-7 cancer cells through an effective PTT/PDT process while subjected to combined laser irradiation (660 and 808 nm). MTT assays were further performed after incubating different times in MCF-7 cells, which confirmed a time-dependent cytotoxicity of APPC and APPFC under combined laser irradiation (Figure S8).

CONCLUSIONS

A facile method was presented to prepare stable, monodisperse, biocompatible eyeball-like yolk−shell nanoparticles using noble metals Au and Pd. Compared with bare Au@Pd NPs, the newly developed APPFC system exhibited higher drug loading capacity, better photothermal efficacy, and higher specificity. By combining photothermal therapy and photodynamic therapy, the APPFC system is an excellent approach for cancer treatment. Importantly, this synthetic method provides a novel approach for the preparation of bimetal nanocomposites for biomedical applications. Besides, this bimetallic therapeutic platform integrates tumor-specific accumulation and a noninvasive therapeutic modality into a system, showing great potential for effective treatment of cancer.

EXPERIMENTAL SECTION

The eyeball-like Au@Pd NPs were synthesized via a three-step method, including synthesizing Au NPs, core−shell Au@Ag NPs, and galvanic displacement reaction employing the Ag shell as the sacrificing template. The Au NPs were synthesized through premixing methods reported elsewhere.[44] Briefly, 1 mL of the $HAuCl_4$ aqueous solution (0.5 wt %) and 42.5 μL of the $AgNO_3$ aqueous solution (0.1 wt %) were added to a given volume of citrate aqueous solution (1 wt %) under stirring. Then, water was added to the mixed solution until the volume was 2.5 mL. After incubation of about 4.5 min, this

https://dx.doi.org/10.1021/acsabm.0c00624
ACS Appl. Bio Mater. 2020, 3, 5922−5929

mixture was quickly poured into 47.5 mL of boiling water in a 100 mL flask. Further reflux of the whole reaction solution was continued for 1 h under stirring to warrant the formation of uniform quasispherical Au NPs. A typical synthesis of core−shell Au@Ag NPs with 12 nm Au core is as follows. Three hundred microliters of aqueous citrate solution (1 wt %) was added into 8.6 mL of water, followed by adding 1 mL of an aqueous solution of as-prepared Au NPs, 20 μL of aqueous HQ solution (0.03 M) and 50 μL of aqueous $AgNO_3$ solution (0.01 M) successively. After stirring for about 4 h, the color of the aqueous solution was changed from light red to orange. Eventually, core−shell Au@Ag NPs with a 6.3 nm Ag shell were obtained. Eyeball-like Au@Pd NPs were fabricated by adding 150 μL of the Na_2PdCl_4 aqueous solution (1 mM) into 10 mL of the obtained aqueous solution of Au@Ag NPs. The reactions were further stirred for about 4 h at room temperature. The color of the aqueous solution changed from orange to brown. The products were centrifuged at 8000 rcf for 10 min and washed two times in turn with de-ionized water.

To form APPFC NPs, the obtained eyeball-like Au@Pd NPs were modified by PEG, FA, and Ce6 step by step. First,10 mg of amino-PEG was dissolved in 0.5 mg mL^{-1} of the Au@Pd NPs solution under sonication and stirring. After several times of water washing, the excess PEG polymers were removed. Subsequently, a solution of Ce6 (2 mg) and 14 mg FA (14 mg) in dimethyl sulfoxide (DMSO, 1 mL) was prepared. Next, 1-ethyl-3-(3-dimethylaminopropyl) carbodiimide hydrochloride (EDC) and *N*-hydroxysuccinimide (NHS) (1:1; 1 mg) were added into the above-obtained Au@Pd-PEG solution. Two solutions are mixed thoroughly and reactions are allowed for 4 h. The Au@Pd-PEG-Ce6 (APPC) NPs were prepared by the same method only without adding FA.

■ ASSOCIATED CONTENT

Supporting Information

The Supporting Information is available free of charge at https://pubs.acs.org/doi/10.1021/acsabm.0c00624.

Additional experimental details, including material; characterization; measurements of drug loading ability; cytotoxicity assay; measurements of ROS generation under laser irradiation at 660 nm; temperature elevation induced by laser irradiation at 808 nm; confocal microscopy studies of the APPFC NPs uptake; photograph of prepared Au@Pd NPs in PBS; photographs of Ce6, FA, Au@Pd-PEG, APPC, and APPFC in PBS; size distribution of Au@Pd-PEG NPs as measured by dynamic light scattering; UV−vis spectra of FA and APPFC in water; CLSM images of MCF-7 cells incubated with APPFC with and without 808 nm laser irradiation (1.5 W cm^{-2}); UV−vis spectra of ABDA at different times under 660 nm laser irradiation; MTT assay of MCF-7 cells incubated with Au@Pd and Au@Pd-PEG (PDF)

■ AUTHOR INFORMATION

Corresponding Authors

Yang Song − *School of Mechanical and Materials Engineering, Washington State University, Pullman, Washington 99164, United States;* orcid.org/0000-0003-0848-4831; Email: yang.song@wsu.edu

Dan Du − *School of Mechanical and Materials Engineering, Washington State University, Pullman, Washington 99164, United States;* orcid.org/0000-0003-1952-4042; Email: annie.du@wsu.edu

Yuehe Lin − *School of Mechanical and Materials Engineering, Washington State University, Pullman, Washington 99164, United States;* orcid.org/0000-0003-3791-7587; Email: yuehe.lin@wsu.edu

Authors

Xiaoli Cai − *School of Mechanical and Materials Engineering, Washington State University, Pullman, Washington 99164, United States*

Shichao Ding − *School of Mechanical and Materials Engineering, Washington State University, Pullman, Washington 99164, United States*

Qiurong Shi − *School of Mechanical and Materials Engineering, Washington State University, Pullman, Washington 99164, United States*

Zhaoyuan Lyu − *School of Mechanical and Materials Engineering, Washington State University, Pullman, Washington 99164, United States*

Dong Liu − *School of Mechanical and Materials Engineering, Washington State University, Pullman, Washington 99164, United States*

Wen-ji Dong − *Gene and Linda Voiland School of Chemical Engineering and Bioengineering, Washington State University, Pullman, Washington 99164, United States*

Min Du − *Laboratory of Nutrigenomics and Growth Biology, Department of Animal Sciences, Washington State University, Pullman, Washington 99164, United States*

Prashanta Dutta − *School of Mechanical and Materials Engineering, Washington State University, Pullman, Washington 99164, United States*

Complete contact information is available at: https://pubs.acs.org/10.1021/acsabm.0c00624

Author Contributions

[‖]X.C. and S.D. contributed equally to this manuscript

Notes

The authors declare no competing financial interest.

■ ACKNOWLEDGMENTS

This work was supported by a WSU start-up fund. The authors would like to acknowledge the helpful discussion with Dr. Ke Chen.

■ REFERENCES

(1) Ward, E. M.; Sherman, R. L.; Henley, S. J.; Jemal, A.; Siegel, D. A.; Feuer, E. J.; Firth, A. U.; Kohler, B. A.; Scott, S.; Ma, J.; Anderson, R. N.; Benard, V.; Cronin, K. Annual Report to the Nation on the Status of Cancer, 1999-2015, Featuring Cancer in Men and Women Ages 20-49. *J. Natl. Cancer Inst.* **2019**, *111*, 1279−1297.

(2) Wang, Y.; Wu, W.; Liu, J.; Manghnani, P. N.; Hu, F.; Ma, D.; Teh, C.; Wang, B.; Liu, B. Cancer-Cell-Activated Photodynamic Therapy Assisted by Cu (II)-Based Metal-Organic Framework. *ACS Nano* **2019**, *13*, 6879−6890.

(3) Xu, Y.; Hu, X.; Guan, P.; Du, C.; Tian, Y.; Ding, S.; Li, Z.; Yan, C. A Novel Controllable Molecularly Imprinted Drug Delivery System Based on the Photothermal Effect of Graphene Oxide Quantum Dots. *J. Mater. Sci.* **2019**, *54*, 9124−9139.

(4) Ding, S.; Khan, A. I.; Cai, X.; Song, Y.; Lyu, Z.; Du, D.; Dutta, P.; Lin, Y. Overcoming Blood-Brain Barrier Transport: Advances in Nanoparticle-Based Drug Delivery Strategies. *Mater. Today* **2020**, DOI: 10.1016/j.mattod.2020.02.001.

(5) Yu, X. N.; Deng, Y.; Zhang, G. C.; Liu, J.; Liu, T. T.; Dong, L.; Zhu, C. F.; Shen, X. Z.; Li, Y. H.; Zhu, J. M. Sorafenib-Conjugated Zinc Phthalocyanine Based Nanocapsule for Trimodal Therapy in an Orthotopic Hepatocellular Carcinoma Xenograft Mouse Model. *ACS Appl. Mater. Interfaces* **2020**, *12*, 17193−17206.

(6) Zhang, X.; Machuki, J. O.; Pan, W. Z.; Cai, W. B.; Xi, Z. Q.; Shen, F. Z.; Zhang, L. J.; Yang, Y.; Gao, F. L.; Guan, M. Carbon Nitride Hollow Theranostic Nanoregulators Executing Laser-Activatable Water Splitting for Enhanced Ultrasound/Fluorescence Imaging and Cooperative Phototherapy. *ACS Nano* **2020**, *14*, 4045−4060.
(7) Ma, Z.; Zhang, M.; Jia, X.; Bai, J.; Ruan, Y.; Wang, C.; Sun, X.; Jiang, X. Fe^{III}-Doped Two-Dimensional C_3N_4 Nanofusiform: a New O_2-Evolving and Mitochondria-Targeting Photodynamic Agent for MRI and Enhanced Antitumor Therapy. *Small* **2016**, *12*, 5477−5487.
(8) Luo, Y.; Li, Z.; Zhu, C.; Cai, X.; Qu, L.; Du, D.; Lin, Y. Graphene-Like Metal-Free 2D Nanosheets for Cancer Imaging and Theranostics. *Trends Biotechnol.* **2018**, *36*, 1145−1156.
(9) Cai, X. L.; Yan, H. Y.; Luo, Y. N.; Song, Y.; Zhao, Y. T.; Li, H.; Du, D.; Lin, Y. H. Mesoporous Carbon Nanospheres with ZnO Nanolids for Multimodal Therapy of Lung Cancer. *ACS Appl. Bio Mater.* **2018**, *1*, 1165−1173.
(10) Luo, Y.; Song, Y.; Wang, M.; Jian, T.; Ding, S.; Mu, P.; Liao, Z.; Shi, Q.; Cai, X.; Jin, H.; et al. Bioinspired Peptoid Nanotubes for Targeted Tumor Cell Imaging and Chemo-Photodynamic Therapy. *Small* **2019**, *15*, No. 1902485.
(11) Deng, W.; Wu, Q.; Sun, P.; Yuan, P.; Lu, X.; Fan, Q.; Huang, W. Zwitterionic Diketopyrrolopyrrole for Fluorescence/Photoacoustic Imaging Guided Photodynamic/Photothermal Therapy. *Polym. Chem.* **2018**, *9*, 2805−2812.
(12) Dong, W.; Li, Y.; Niu, D.; Ma, Z.; Gu, J.; Chen, Y.; Zhao, W.; Liu, X.; Liu, C.; Shi, J. Facile Synthesis of Monodisperse Superparamagnetic Fe_3O_4 Core@Hybrid@Au Shell Nanocomposite for Bimodal Imaging and Photothermal Therapy. *Adv. Mater.* **2011**, *23*, 5392−5397.
(13) Wang, J.; Tan, X.; Pang, X.; Liu, L.; Tan, F.; Li, N. MoS_2 Quantum Dot@Polyaniline Inorganic-Organic Nanohybrids for in Vivo Dual-Modal Imaging Guided Synergistic Photothermal/Radiation Therapy. *ACS Appl. Mater. Interfaces* **2016**, *8*, 24331−24338.
(14) Wagner, V.; Dullaart, A.; Bock, A.-K.; Zweck, A. The Emerging Nanomedicine Landscape. *Nat. Biotechnol.* **2006**, *24*, 1211−1217.
(15) Riehemann, K.; Schneider, S. W.; Luger, T. A.; Godin, B.; Ferrari, M.; Fuchs, H. Nanomedicine-Challenge and Perspectives. *Angew. Chem., Int. Ed.* **2009**, *48*, 872−897.
(16) Jaque, D.; Martinez Maestro, L.; del Rosal, B.; Haro-Gonzalez, P.; Benayas, A.; Plaza, J. L.; Martin Rodriguez, E.; Garcia Sole, J. Nanoparticles for Photothermal Therapies. *Nanoscale* **2014**, *6*, 9494−9530.
(17) Song, Y.; Shi, Q. R.; Zhu, C. Z.; Luo, Y. N.; Lu, Q.; Li, H.; Ye, R. F.; Du, D.; Lin, Y. H. Mitochondrial-Targeted Multifunctional Mesoporous Au@Pt Nanoparticles for Dual-Mode Photodynamic and Photothermal Therapy of Cancers. *Nanoscale* **2017**, *9*, 15813−15824.
(18) Ma, Y.; Liang, X.; Tong, S.; Bao, G.; Ren, Q.; Dai, Z. Gold Nanoshell Nanomicelles for Potential Magnetic Resonance Imaging, Light-Triggered Drug Release, and Photothermal Therapy. *Adv. Funct. Mater.* **2013**, *23*, 815−822.
(19) Wang, S.; Huang, P.; Nie, L.; Xing, R.; Liu, D.; Wang, Z.; Lin, J.; Chen, S.; Niu, G.; Lu, G.; Chen, X. Single Continuous Wave Laser Induced Photodynamic/Plasmonic Photothermal Therapy Using Photosensitizer-Functionalized Gold Nanostars. *Adv. Mater.* **2013**, *25*, 3055−3061.
(20) Wang, W.; Hao, C.; Sun, M.; Xu, L.; Xu, C.; Kuang, H. Spiky Fe_3O_4@Au Supraparticles for Multimodal in Vivo Imaging. *Adv. Funct. Mater.* **2018**, *28*, No. 1800310.
(21) Yang, Z.; Du, Y.; Sun, Q.; Peng, Y.; Wang, R.; Zhou, Y.; Wang, Y.; Zhang, C.; Qi, X. Albumin-Based Nanotheranostic Probe with Hypoxia Alleviating Potentiates Synchronous Multimodal Imaging and Phototherapy for Glioma. *ACS Nano* **2020**, *14*, 6191−6212.
(22) Lee, S. Y.; Shieh, M. J. Platinum(II) Drug-Loaded Gold Nanoshells for Chemo-Photothermal Therapy in Colorectal Cancer. *ACS Appl. Mater. Interfaces* **2020**, *12*, 4254−4264.
(23) Xiang, S.; Wang, D.; Zhang, K.; Liu, W.; Wu, C.; Meng, Q.; Sun, H.; Yang, B. Chelation Competition Induced Polymerization (CCIP): Construction of Integrated Hollow Polydopamine Nanocontainers with Tailorable Functionalities. *Chem. Commun.* **2016**, *52*, 10155−10158.
(24) Luan, J.; Liu, K. K.; Tadepalli, S.; Jiang, Q.; Morrissey, J. J.; Kharasch, E. D.; Singamaneni, S. PEGylated Artificial Antibodies: Plasmonic Biosensors with Improved Selectivity. *ACS Appl. Mater. Interfaces* **2016**, *8*, 23509−23516.
(25) Zhang, Y.; Lv, F.; Cheng, Y.; Yuan, Z.; Yang, F.; Liu, C.; Cao, Y.; Zhang, K.; Lu, H.; Zada, S. Pd@Au Bimetallic Nanoplates Decorated Mesoporous MnO_2 for Synergistic Nucleus-Targeted NIR-II Photothermal and Hypoxia-Relieved Photodynamic Therapy. *Adv. Healthcare Mater.* **2020**, *9*, No. 1901528.
(26) Zhang, L.; Li, S.; Chen, X.; Wang, T.; Li, L.; Su, Z.; Wang, C. Tailored Surfaces on 2D Material: UFO-Like Cyclodextrin-Pd Nanosheet/Metal Organic Framework Janus Nanoparticles for Synergistic Cancer Therapy. *Adv. Funct. Mater.* **2018**, *28*, No. 1803815.
(27) Zou, H.; Wang, R.; Dai, J.; Wang, Y.; Wang, X.; Zhang, Z.; Qiu, S. Amphiphilic Hollow Porous Shell Encapsulated Au@Pd Bimetal Nanoparticles for Aerobic Oxidation of Alcohols in Water. *Chem. Commun.* **2015**, *51*, 14601−14604.
(28) Zhang, N.; Mei, K.; Guan, P.; Hu, X.; Zhao, Y. Protein-Based Artificial Nanosystems in Cancer Therapy. *Small* **2020**, *16*, No. 1907256.
(29) Jia, Y.; Song, Y.; Qu, Y.; Peng, J.; Shi, K.; Du, D.; Li, H.; Lin, Y.; Qian, Z. Mesoporous PtPd Nanoparticles for Ligand-Mediated and Imaging-Guided Chemo-Photothermal Therapy of Breast Cancer. *Nano Res.* **2020**, *13*, 1739−1748.
(30) Kim, K.; Oh, K. S.; Park, D. Y.; Lee, J. Y.; Lee, B. S.; Kim, I. S.; Kim, K.; Kwon, I. C.; Sang, Y. K.; Yuk, S. H. Doxorubicin/Gold-Loaded Core/Shell Nanoparticles for Combination Therapy to Treat Cancer Through the Enhanced Tumor Targeting. *J. Controlled Release* **2016**, *228*, 141−149.
(31) Song, Y.; Wang, M.; Li, S.; Jin, H.; Cai, X.; Du, D.; Li, H.; Chen, C. L.; Lin, Y. Efficient Cytosolic Delivery Using Crystalline Nanoflowers Assembled from Fluorinated Peptoids. *Small* **2018**, *14*, No. 1803544.
(32) Zhang, N.; Zhang, N.; Xu, Y.; Li, Z.; Yan, C.; Mei, K.; Ding, M.; Ding, S.; Guan, P.; Qian, L.; Du, C.; Hu, X. Molecularly Imprinted Materials for Selective Biological Recognition. *Macromol. Rapid Commun.* **2019**, *40*, No. 1900096.
(33) Blanco, E.; Shen, H.; Ferrari, M. Principles of Nanoparticle Design for Overcoming Biological Barriers to Drug Delivery. *Nat. Biotechnol.* **2015**, *33*, 941−951.
(34) Wang, H.; Sui, H.; Zheng, Y.; Jiang, Y.; Shi, Y.; Liang, J.; Zhao, L. Curcumin-Primed Exosomes Potently Ameliorate Cognitive Function in AD Mice by Inhibiting Hyperphosphorylation of the Tau Protein Through the AKT/GSK-3beta Pathway. *Nanoscale* **2019**, *11*, 7481−7496.
(35) Butcher, N. J.; Mortimer, G. M.; Minchin, R. F. Drug Delivery: Unravelling the Stealth Effect. *Nat. Nanotechnol.* **2016**, *11*, 310.
(36) Roh, K.-H.; Martin, D. C.; Lahann, J. Biphasic Janus Particles with Nanoscale Anisotropy. *Nat. Mater.* **2005**, *4*, 759−763.
(37) Zhang, H.; Huang, X.; Noonan, O.; Zhou, L.; Yu, C. Tailored Yolk-Shell Sn@C Nanoboxes for High-Performance Lithium Storage. *Adv. Funct. Mater.* **2017**, *27*, No. 1606023.
(38) Gao, X.; Yue, Q.; Liu, Z.; Ke, M.; Zhou, X.; Li, S.; Zhang, J.; Zhang, R.; Chen, L.; Mao, Y.; Li, C. Guiding Brain-Tumor Surgery via Blood-Brain-Barrier-Permeable Gold Nanoprobes with Acid-Triggered MRI/SERRS Signals. *Adv. Mater.* **2017**, *29*, No. 1603917.
(39) Mandal, S.; Roy, D.; Chaudhari, R.; Sastr, M. Pt and Pd Nanoparticles Immobilized on Amine-Functionalized Zeolite: Excellent Catalysts for Hydrogenation and Heck Reactions. *Chem. Mater.* **2004**, *16*, 3714−3724.
(40) Cai, X.; Luo, Y.; Song, Y.; Liu, D.; Yan, H.; Li, H.; Du, D.; Zhu, C.; Lin, Y. Integrating in situ Formation of Nanozymes with Three-Dimensional Dendritic Mesoporous Silica Nanospheres for Hypoxia-Overcoming Photodynamic therapy. *Nanoscale* **2018**, *10*, 22937−22945.

https://dx.doi.org/10.1021/acsabm.0c00624
ACS Appl. Bio Mater. 2020, 3, 5922−5929

(41) Low, P. S.; Henne, W. A.; Doorneweerd, D. D. Discovery and Development of Folic-Acid-Based Receptor Targeting for Imaging and Therapy of Cancer and Inflammatory Diseases. *Acc. Chem. Res.* **2008**, *41*, 120−129.
(42) Majd, M. H.; Barar, J.; Asgari, D.; Valizadeh, H.; Rashidi, M. R.; Kafil, V.; Shahbazi, J.; Omidi, Y. Targeted Fluoromagnetic Nanoparticles for Imaging of Breast Cancer MCF-7 Cells. *Adv. Pharm. Bull.* **2013**, *3*, 189−195.
(43) Hoye, A. T.; Davoren, J. E.; Wipf, P.; Fink, M. P.; Kagan, V. E. Targeting Mitochondria. *Acc. Chem. Res.* **2008**, *41*, 87−97.
(44) Shi, Q.; Zhang, P.; Li, Y.; Xia, H.; Wang, D.; Tao, X. Synthesis of Open-Mouthed, Yolk-Shell Au@AgPd Nanoparticles with Access to Interior Surfaces for Enhanced Electrocatalysis. *Chem. Sci.* **2015**, *6*, 4350−4357.

https://dx.doi.org/10.1021/acsabm.0c00624
ACS Appl. Bio Mater. 2020, 3, 5922−5929